






# Numerical analysis of flow anisotropy in rotated-square deterministic lateral displacement devices at moderate Reynolds number

Calum Mallorie <sup>1</sup>, Rohan Vernekar <sup>2</sup>, Benjamin Owen <sup>1</sup>,  
David W. Inglis <sup>3</sup> and Timm Krüger <sup>1</sup>

<sup>1</sup>*School of Engineering, Institute for Multiscale Thermo-fluids, University of Edinburgh, King's Buildings, Edinburgh EH9 3FB, United Kingdom*

<sup>2</sup>*Université Grenoble Alpes, CNRS, LRP, 38000 Grenoble, France*

<sup>3</sup>*School of Engineering, Macquarie University, Sydney, NSW 2109, Australia*



(Received 27 September 2023; accepted 19 December 2023; published 21 February 2024)

Deterministic lateral displacement (DLD) is a microfluidic method for accurately separating particles by size or deformability. Recent efforts to operate DLD devices in the inertial, rather than in the Stokes flow regime, have been hindered by a loss of separation efficiency and difficulty predicting the separation behavior. One factor contributing to these problems is the onset of inertia-induced flow anisotropy where the average flow direction does not align with the direction of the pressure gradient in the device. We use the lattice-Boltzmann method to simulate two-dimensional flow through a rotated-square DLD geometry with circular pillars at a Reynolds number up to 100 for different gap sizes and rotation angles. We find that anisotropy in this geometry is a nonmonotonous function of Reynolds number and can be positive or negative. This finding is in contradiction to the naive expectation that inertia would always drive flow along the principal direction of the pillar array. Anisotropy tends to increase in magnitude with gap size and rotation angle. By analyzing the traction distribution along the pillar surface, we explain how the change of the flow field upon increasing inertia leads to the observed trends of anisotropy. Our work contributes to a better understanding of the inertial flow behavior in ordered cylindrical porous media, and it might contribute to improved DLD designs for operation in the inertial regime.

DOI: [10.1103/PhysRevFluids.9.024203](https://doi.org/10.1103/PhysRevFluids.9.024203)

## I. INTRODUCTION

Particle separation based on physical properties is an essential process in medical diagnostics and drug development. Microfluidic techniques, including deterministic lateral displacement (DLD), have gained prominence due to their high size resolution and throughput compared to traditional methods like filtration and centrifugation [1]. DLD was originally proposed by Huang *et al.* [2], and it has been successfully applied to the separation of various biological particles by their mechanical phenotype [3,4], with a size resolution down to 10 nm [2].

DLD operates by dividing a laminar fluid flow into flow lanes that are bounded by stagnation streamlines, which originate and terminate at the surface of pillars arranged in a periodic array of obstacles [5]; see Fig. 1. To leading order, particles follow streamlines and, therefore, remain in the same flow lane, unless forced out by contact with an obstacle. If a particle is larger than

---

*Published by the American Physical Society under the terms of the [Creative Commons Attribution 4.0 International](https://creativecommons.org/licenses/by/4.0/) license. Further distribution of this work must maintain attribution to the author(s) and the published article's title, journal citation, and DOI.*

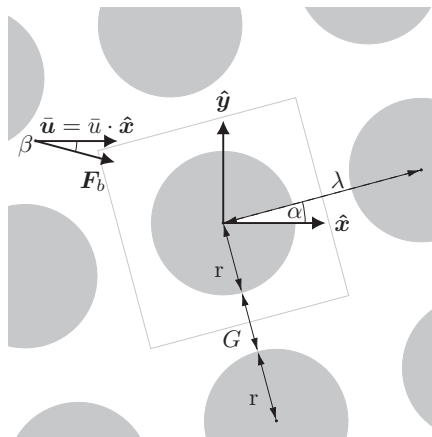


FIG. 1. Illustration of the rotated-square array. The circular pillars of radius  $r$  lie on the nodes of a square lattice with center-to-center distance  $\lambda$ . The gap size between pillars is  $G = \lambda - 2r$ . The array is rotated at an angle  $\alpha$  relative to the coordinate axes. By varying the direction of the body force density driving the flow, which is denoted  $F_b$ , the average velocity of the fluid  $\bar{u}$  is imposed to be parallel to the basis vector  $\hat{x}$ , which indicates the axis of the DLD device. For the validation test presented in Sec. III A,  $\alpha$  is set to zero and the body force  $F_b$  is maintained at an angle  $\beta$ . Simulations are carried out over one unit cell of the array with periodic boundary conditions, highlighted by the gray box.

a critical radius  $r_c$ , determined by the width of the flow lane adjacent to a pillar, contact with a pillar surface forces the hydrodynamic center of the particle into a neighboring flow lane. This process occurs at each subsequent pillar, leading to lateral migration across streamlines. Particles smaller than  $r_c$  remain in their flow lane and travel in the same direction as the bulk fluid flow. The different modes of transport through the DLD device have different angles of displacement relative to the flow field, and different particles can be collected at separate downstream outlets.

DLD has been shown to be highly effective in the Stokes regime, with separation efficiencies approaching 100% in some cases [6,7]. The behavior of the devices in this regime has been well characterized, with predictive empirical relations [8] and design heuristics [9] developed. However, operating devices in the Stokes regime limits the sample throughput due to the necessarily low flow rates.

Operating DLD devices with higher flow rates requires larger flow speed, which leads to the onset of inertial effects. DLD devices operating in the inertial regime show a reduction of the critical size [10–12], which is useful to prevent clogging. However, inertia also leads to additional effects, such as a breakdown of the separation efficiency [13], loss of symmetry in the flow field [12,14], and increased influence of the particle-fluid density difference [15].

In some examples of DLD operating at high flow rates, there is evidence that the average flow direction tilts to align with the array inclination as the flow rate is increased [16,17]. A likely cause of this problem is anisotropic fluid conduction in the array [16]. Anisotropy is the tendency of the fluid flow to deviate from the direction of the applied pressure gradient. Anisotropy can cause changes to the average flow direction, which changes the critical size in the array in complex ways and causes a breakdown of separation performance [18,19]. DLD devices with circular pillars arranged in a rotated-square layout (Fig. 1) have zero anisotropy in the Stokes regime [20], and they are therefore recommended as best practice [21]. Under the influence of inertia, however, rotated-square layouts have been shown to exhibit anisotropy [22]. The mechanisms leading to the increase in anisotropy with fluid inertia in DLD geometries should be better understood to enable improved designs of inertial DLD devices.

Flows through DLD-like cylindrical pillar arrays have been historically investigated in the field of ordered porous media studies [23,24], which have numerous industrial [25,26], biological [27], and geological [28] applications. Most of these studies choose pillar array alignment of either  $0^\circ$  or  $45^\circ$  to the driving pressure gradient, ensuring flow symmetry in steady state, with a strong interest in measuring the flow resistance (or permeability) of the arrays [29–34]. As far as we are aware, only Koch and Ladd [22] have examined the effect of fluid inertia on flow permeability of inclined cylindrical pillar arrays. Using two-dimensional lattice-Boltzmann simulations, Koch and Ladd found that rotated-square arrays show anisotropic permeability due to fluid inertia. Remarkably, they observed that the anisotropy can become negative for certain configurations, meaning that the flow chooses to tilt against the inclination of the pillar array, due to fluid inertia. Koch and Ladd [22] did not explain the physical reasons for this counterintuitive behavior.

In this work, we use a two-dimensional (2D) lattice-Boltzmann method to simulate inertial flow in rotated-square DLD devices. We investigate the emergence of anisotropy as a function of Reynolds number, gap size, and array inclination angle. Our results confirm that anisotropy is a nonmonotonous function of Reynolds number and can be positive or negative. The magnitude of anisotropy generally increases with gap size and array inclination. By analyzing the distribution of the traction vector along the pillar surface, we explain the observed behavior of the anisotropy.

## II. MODEL AND METHODS

### A. Physical and mathematical model

We investigate the flow of a Newtonian, incompressible fluid through a rotated-square DLD device in two dimensions (Fig. 1). We consider a portion of the device far from the walls that confine the DLD device. Circular pillars of radius  $r$  are arranged in a periodically repeating square array with center-to-center distance  $\lambda$ . The minimum gap size between pillar surfaces is  $G = \lambda - 2r$ . The array is tilted at an angle  $\alpha$  counterclockwise with respect to the device axis. The no-slip condition holds at the surface of the pillars, and periodic boundary conditions are applied to the simulation domain.

We define the unit basis vectors  $\hat{x}$  and  $\hat{y}$  to point tangentially and orthogonally to the axis of the DLD device. The average flow direction  $\bar{\mathbf{u}}$  is aligned with the  $x$ -axis,

$$\bar{\mathbf{u}} = \bar{u} \cdot \hat{x}, \quad (1)$$

as would be expected in a real-world device. The flow is driven by a body force density (force per unit area in two dimensions)  $\mathbf{F}_b$ , whose direction is set such that Eq. (1) holds [20]. We only consider cases for which the flow field becomes steady after some time, which, for given values of  $G$  and  $\alpha$ , happens at sufficiently low Reynolds number.

### B. Drag and lift forces and flow anisotropy

The fluid stress tensor  $\boldsymbol{\sigma}$ , including inertial, pressure, and viscous contributions, can be expressed using index notation as

$$\sigma_{ij} = -\rho u_i u_j - p \delta_{ij} + \rho \nu (\partial_i u_j + \partial_j u_i), \quad (2)$$

where  $\rho$  is the density,  $\nu$  is the kinematic viscosity,  $u_i$  is the  $i$ -component of the fluid velocity,  $p$  is the pressure, and  $\delta_{ij}$  is the Kronecker symbol. On the pillar surface  $S$ , the inertial contribution,  $\rho u_i u_j$ , vanishes due to the no-slip condition:

$$\sigma_{ij}|_S = -p \delta_{ij} + \rho \nu (\partial_i u_j + \partial_j u_i). \quad (3)$$

The traction vector  $\mathbf{t}$  at any point on  $S$  can be calculated by projecting the stress tensor onto the surface normal vector  $\hat{\mathbf{n}}$  which, by definition, points into the fluid:

$$\mathbf{t} = \boldsymbol{\sigma}|_S \cdot \hat{\mathbf{n}}. \quad (4)$$

Note that  $\mathbf{t}$  is defined in such a way that the traction vector is the force exerted by the fluid on the pillar surface, rather than the other way around.

At steady state, the momentum balance dictates that the integral of the traction vector over the surface  $S$  of one pillar is equal to the integral of the body force driving the fluid flow over the area  $A$  of one unit cell of the array:

$$\mathbf{F} := \int_A \mathbf{F}_b dA = \oint_S \mathbf{t} dS. \quad (5)$$

The local drag and lift force densities acting on a pillar surface element  $dS$  are the components of the traction vector pointing in the direction of, and orthogonally to, the average flow direction, respectively:

$$f_d = \mathbf{t} \cdot \hat{\mathbf{x}}, \quad f_l = \mathbf{t} \cdot \hat{\mathbf{y}}. \quad (6)$$

The total force acting on the pillar can be decomposed into net drag and lift forces,  $\mathbf{F} = F_d \hat{\mathbf{x}} + F_l \hat{\mathbf{y}}$ , where

$$F_d = \oint_S f_d dS, \quad F_l = \oint_S f_l dS. \quad (7)$$

Note that  $F_d$  is always positive, and  $F_l$  can be positive, negative, or zero.

A flow configuration for which  $F_l = 0$  holds for any angle  $\alpha$  is called isotropic: the average flow  $\bar{\mathbf{u}}$  and the total force vector  $\mathbf{F}_b$  are always parallel, and no lateral flow deflection occurs. The prime example for an isotropic flow is the Stokes flow (zero Reynolds number) over a square array of circular obstacles [20]. Isotropy can be broken by choosing different pillar shapes, pillar arrangements, or by having a finite Reynolds number [20,22,35]. We define flow anisotropy as the dimensionless ratio of lift over drag:

$$A = -\frac{F_l}{F_d}. \quad (8)$$

The negative sign is to match the convention established in previous work [20]. Positive anisotropy,  $A > 0$ , indicates that the flow would be deflected in a counterclockwise fashion (along the positive  $y$ -axis). However, in a real device, fluid would not be able to accumulate at the side walls due to incompressibility of the fluid, and instead a lateral pressure gradient would build up that maintains the average flow along the  $x$ -axis. In our model, this pressure gradient is captured by the  $y$ -component of the body force density  $\mathbf{F}_b$ , which is obtained in such a way that Eq. (1) holds at any time. The resulting force components  $F_d$  and  $F_l$  then determine  $A$ .

For further analysis, we also define the contributions to flow anisotropy coming from the normal and shear components of the traction vector, respectively:

$$A = A^n + A^s, \quad A^n = -\frac{F_1^n}{F_d}, \quad A^s = -\frac{F_1^s}{F_d}, \quad (9)$$

where

$$F_1^n = \oint_S \mathbf{t}^n \cdot \hat{\mathbf{y}} dS, \quad F_1^s = \oint_S \mathbf{t}^s \cdot \hat{\mathbf{y}} dS, \quad (10)$$

where

$$\mathbf{t}^n = (\mathbf{t} \cdot \hat{\mathbf{n}})\hat{\mathbf{n}}, \quad \mathbf{t}^s = \mathbf{t} - \mathbf{t}^n \quad (11)$$

are the normal and shear components of the traction vector. While  $A^s$  is determined by the viscous shear stress at the pillar surface,  $A^n$  follows from the viscous normal stress and the pressure at the pillar surface.

### C. Dimensionless numbers

Apart from the nondimensionalized gap size  $G^* = G/\lambda$  and the array tilt angle  $\alpha$ , the problem is fully characterized by the Reynolds number  $\text{Re}$ . We define  $\text{Re}$  by the average flow velocity  $\bar{u}$  in the fluid domain excluding the pillars, the pillar diameter  $2r$ , and the kinematic viscosity  $\nu$ , similarly to Koch and Ladd [22]:

$$\text{Re} = \frac{2\bar{u}r}{\nu}. \quad (12)$$

It is also useful to define the packing fraction of the pillars as  $\phi = 1 - \pi \frac{r^2}{\lambda^2}$ . On a macroscopic level, the converged flow is fully described by the resulting anisotropy  $A$  (and its contributions  $A^n$  and  $A^s$ ).

### D. Numerical model and simulation parameters

The 2D fluid flow is solved using the lattice-Boltzmann (LB) method on a D2Q9 lattice [36,37]. We use the BGK collision operator [38] and the Guo forcing scheme [39]. The simple bounce-back method [40] recovers the no-slip boundary condition at the surface of the pillar; this leads to a staircase approximation for all curved boundary surfaces. The kinematic viscosity is set by the lattice-Boltzmann relaxation time,  $\tau$  [36]:

$$\nu = c_s^2 \left( \tau - \frac{\Delta t}{2} \right), \quad (13)$$

where  $c_s = (1/\sqrt{3})\Delta x/\Delta t$  is the speed of sound,  $\Delta x$  is the lattice spacing, and  $\Delta t$  is the time step. To ensure that the assumption of flow incompressibility is met and that the incompressibility error is small, the maximum velocity in our simulations is limited to  $0.03\Delta x/\Delta t$  across all simulations ( $u_{\max}/c_s < 0.05$ ) [36].

The simulation domain is one periodic unit cell of the DLD array, shown by the gray box in Fig. 1. The simulation frame is converted to the physical frame by a clockwise rotation of  $\alpha$ .

To impose the average direction of the velocity field  $\bar{\mathbf{u}} = \bar{u}\hat{\mathbf{x}}$  and its desired magnitude  $\bar{u}$ , the body force density  $\mathbf{F}_b$  is determined iteratively. Only steady cases are considered here, and simulations are stopped when the flow has converged with a tolerance of  $10^{-8}$  calculated from the  $L_2$  norm of the difference of the flow fields at times  $t$  and  $t - 1000\Delta t$ .

To ensure that the fluid flow and obstacle surface shape are approximated with sufficient accuracy, we carried out convergence studies [Fig. 2(a)]. We found that a domain size of  $200 \times 200$  grid points is sufficient. In the following, all reported results have been obtained on a lattice with  $200 \times 200$  grid points, corresponding to  $\lambda = 200\Delta x$ .

### E. Obtaining the fluid stress on the pillar surface

Calculation of the traction vector acting on the pillar surface by Eq. (4) requires knowledge of the fluid stress tensor on the surface. We use an interpolation-extrapolation scheme to obtain the fluid stress tensor on the pillar surface.

We discretize the cylinder surface as a series of  $N$  evenly spaced points with separation  $\approx \Delta x$  such that  $2\pi r \approx N\Delta x$ . For each of the  $N$  surface points, we define two points along the surface normal vector at a distance of  $\Delta r$  and  $2\Delta r$ , where we use  $\Delta r = 2\Delta x$ . Bilinear interpolation is used to find the fluid stress tensor at these two points using the four fluid nodes delineating the fluid voxel in which the interpolation point resides. Linear extrapolation from the two points is used to determine the fluid stress tensor at each of the  $N$  surface points. Figure 10, in the Appendix, illustrates this graphically. The fluid stress tensor is then smoothed by computing a five-point moving average along the cylinder surface to reduce noise from the interpolation.

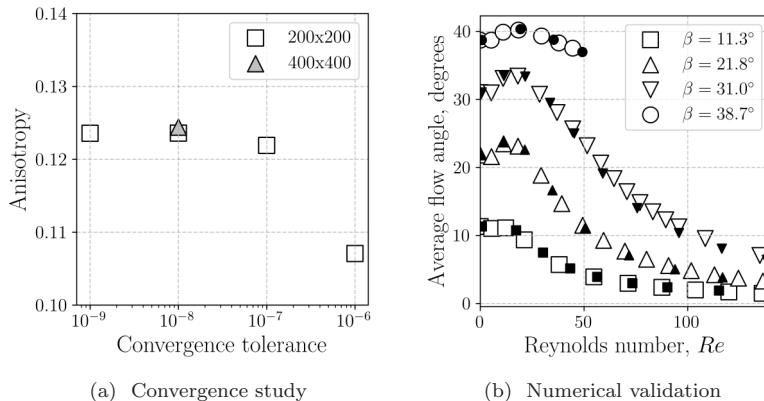


FIG. 2. (a) Study of convergence tolerance and grid independence with  $G^* = 0.5$ ,  $Re = 50$ . Doubling the resolution to  $400 \times 400$  grid points increases the anisotropy by 0.65% at a convergence tolerance of  $10^{-8}$  between times  $t$  and  $t - 1000\Delta t$ . (b) Average flow direction relative to the array orientation at  $G^* = 0.51$  against  $Re$ , for simulations with the flow allowed to freely develop (body force at an angle  $\beta$  with respect to  $\hat{x}$ ). In black are the simulation results obtained by Koch and Ladd [22].

### III. RESULTS AND DISCUSSION

#### A. Validation: comparison with earlier work

To validate our simulations, we compare with the results obtained by Koch and Ladd [22], who investigated the behavior of fluid flow over periodic square arrays of cylinders with  $G^* = 0.51$ , at moderate inertia, using a similar numerical procedure to that presented in this work. Koch and Ladd did not impose a specific flow direction (as we do in the present study), but rather imposed a body force with fixed direction  $\beta$  on an unrotated lattice ( $\alpha = 0$ ) and then measured the resulting average flow direction. Using the same setup, we obtain similar results, as shown in Fig. 2(b). Note that for the forcing angle  $\beta = 38.7^\circ$ , Koch and Ladd found unsteady flows at  $Re > 50$ , which we also confirm. However, we focus on steady flows in the remainder of the present study.

The parameters for all remaining simulations are summarized in Table I.

#### B. Flow field and velocity profiles

Figure 3 shows streamlines and velocity magnitudes for simulations with  $G^* = 0.2, 0.4$ , and  $0.6$ ,  $\alpha = 5^\circ$ , and  $Re = 0.1$  and  $100$ . While the flow field is point symmetric about the center of the pillar for small  $Re$ , a recirculating wake is visible downstream from the pillar at higher  $Re$ , becoming more pronounced with increasing  $G^*$ . The fluid speed is much lower in the recirculation zones, with the majority of fluid flow concentrated in the horizontal gap between pillars, and in a high velocity stream flowing downwards (negative  $y$ -direction) between the recirculation zone and the adjacent downstream pillar.

Figure 4 depicts the velocity profiles for  $\alpha = 5^\circ$  and different values of  $Re$  and  $G^*$  in the gap between pillars as indicated by the red lines in Fig. 3. While the velocity profile is symmetric and

TABLE I. Simulation parameters and associated dimensionless numbers. All quantities are expressed in simulation units ( $\Delta x = 1$  and  $\Delta t = 1$ ).

$Re$ (–)	$G^*$ (–)	$\alpha$ (deg)	$\tau$	$\nu$	$\bar{u}$
[0.1, 100]	0.2, 0.4, 0.6	1, 3, 5	0.55	1/60	$[10^{-5}, 0.02]$

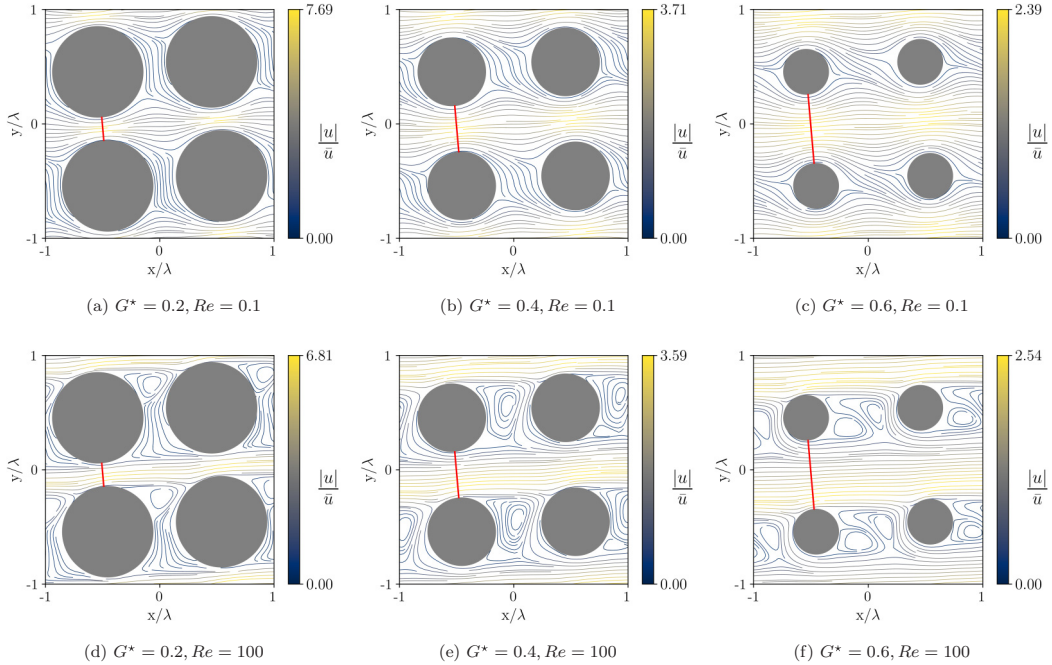


FIG. 3. Streamlines colored by the normalized velocity magnitude (see the right color bar) for different  $G^*$  at  $\alpha = 5^\circ$ . At low  $Re$  (a)–(c), the flow field is symmetrical and attached to pillar surfaces. At higher  $Re$  (d)–(f), a recirculating wake is visible downstream from the pillar. The red line illustrates the path over which the velocity profiles in Fig. 4 are sampled. Note that four periodic unit cells (and therefore four pillars) are shown for visual clarity.

nearly parabolic for  $Re = 0.1$  (near Stokes regime) for all studied values of  $G^*$ , increasing  $Re$  leads to the velocity profile being skewed and pushed against the bottom of the confining gap (in the negative  $y$ -direction), thus the flow speed above the pillar is higher than below. This skewing effect becomes stronger with increasing  $G^*$  and  $\alpha$  (data for other angles not shown) and is caused by the inertia of the fluid, which is forced to flow, on average, along the  $x$ -axis.

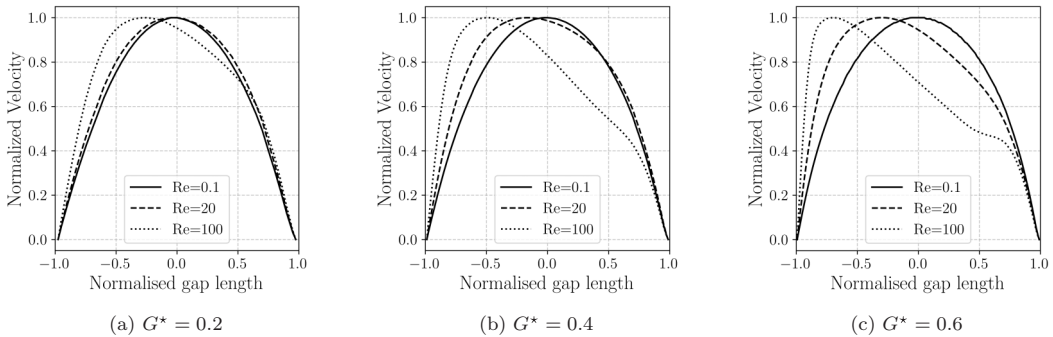


FIG. 4. Velocity profiles along the vertical center-to-center line (shown as a red line in Fig. 3) for  $\alpha = 5^\circ$  and different values of  $G^*$  and  $Re$ . The  $x$ -axis is normalized such that the top side of the pillar corresponds to  $-1$  and the bottom side of the neighboring pillar to  $+1$ . The  $y$ -axis is normalized by the value of the maximum velocity magnitude.

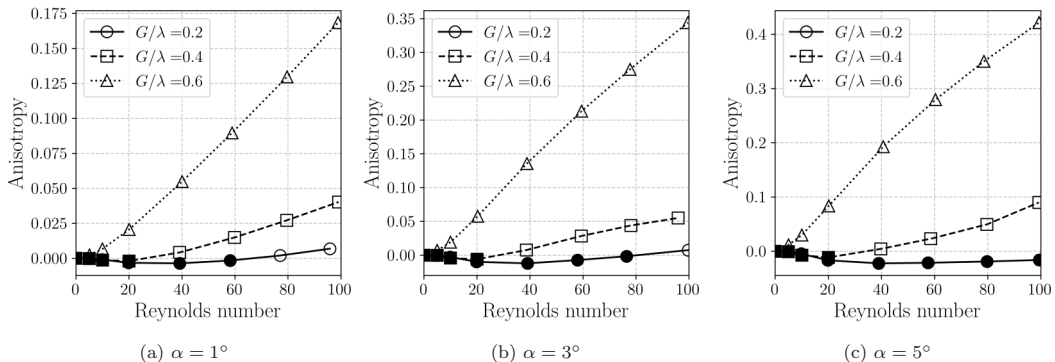


FIG. 5. Anisotropy  $A$  for different values of  $G^*$ ,  $\alpha$ , and  $Re$ . Results are grouped by the value of  $\alpha$  to highlight the similarity of the results for different values of  $\alpha$ . Note that the scale of the y-axis changes between panels. Points for which the anisotropy is negative are marked with filled shapes.

### C. Flow anisotropy

Figure 5 illustrates the anisotropy  $A$  as a function of  $Re$  for various values of reduced gap size  $G^*$  and array inclination angle  $\alpha$ . As expected, anisotropy tends towards zero for  $Re \rightarrow 0$  across all configurations. For  $Re > 5$ , anisotropy becomes significant as inertial effects start to play an important role.

The behavior of anisotropy also depends on gap size. For the largest gap size,  $G^* = 0.6$ , anisotropy grows strongly with  $Re$ , indicating that the fluid prefers to flow along the principal axis of the array. The magnitude of anisotropy also tends to grow with increasing gap size. This is consistent with expectations, as the drag force at a given Reynolds number will be smaller for larger gaps. If the lift were constant, the magnitude of the anisotropy would increase with decreasing gap size according to Eq. (8).

For smaller gaps ( $G^* = 0.4$  and  $0.2$ ), anisotropy exhibits complex behavior. As noted by Koch and Ladd [22], anisotropy first becomes negative before increasing again at larger  $Re$ . Particularly for the smallest gap size,  $G^* = 0.2$ , and the largest array inclination angle,  $\alpha = 5^\circ$ , the anisotropy is negative for all Reynolds numbers studied.

Our results further reveal that the reversal of the direction of the lift force at intermediate  $Re$  occurs even at much smaller angles than those investigated by Koch and Ladd.

The contributions to the anisotropy from the normal and shear components of the traction vector are shown in Figs. 6(a)–6(c) and 6(d)–6(f), respectively. It is evident from these data that both contributions are of similar magnitude, hence neither can be neglected when analyzing the mechanisms that lead to the overall behavior. The data further demonstrates that shear forces always contribute positively to the total anisotropy and increase monotonically with gap size. Thus, as seen in Figs. 6(a)–6(c), normal contributions are the sole source of the negative anisotropy observed for smaller gap sizes. There appear to be at least two competing  $Re$ -dependent mechanisms that determine the contribution of normal forces to the anisotropy, with the negative contributions dominating at intermediate values of  $Re$ , thus leading to the minimum, and negative values, of  $A$ . To understand these observations better, we need to look into the distribution of traction and lift along the pillar surface.

### D. Link between local lift profiles and anisotropy

To understand the mechanisms leading to the onset of anisotropy and its dependency on  $Re$  for a given geometry ( $G^*$  and  $\alpha$ ), we investigate the local forces acting on the pillar surface. Apart from



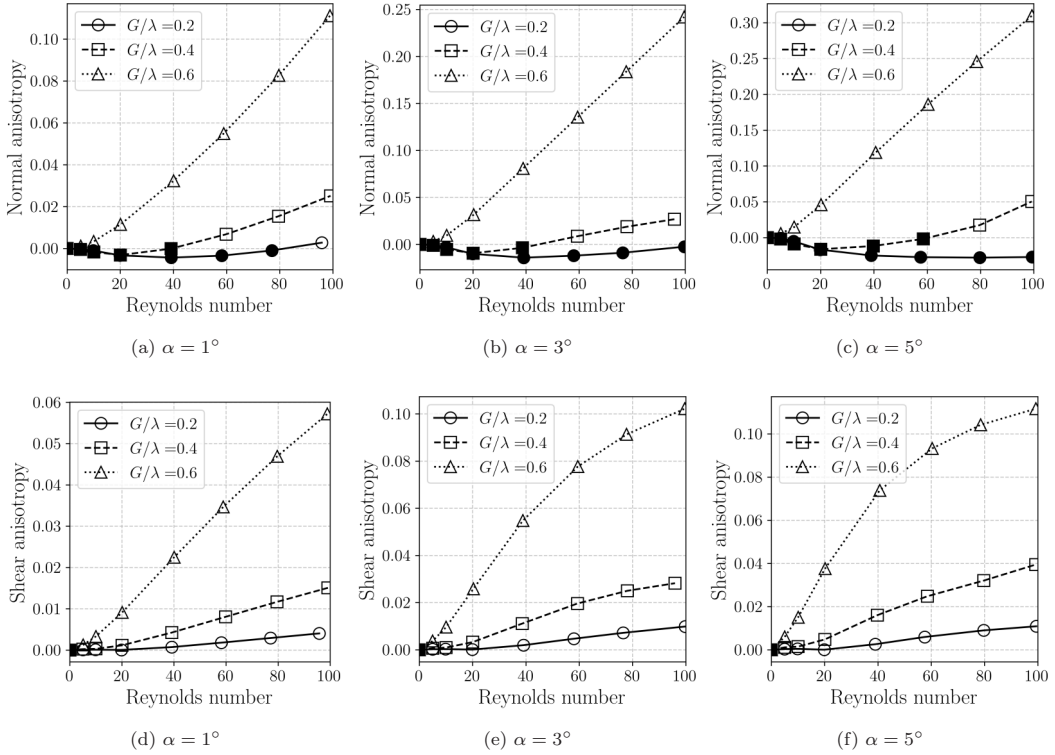


FIG. 6. (a)–(c) Normal and (d)–(f) shear contributions to anisotropy for the simulations shown in Fig. 5. Points for which the anisotropy is below zero are marked with filled shapes.

the upstream ( $x < 0$ ), downstream ( $x > 0$ ), bottom ( $y < 0$ ), and top ( $y > 0$ ) sides of the pillar, we define four quadrants for convenience [see the annotation of Fig. 7(a)]:

Bottom left (BL):  $x < 0, y < 0$ .

Top left (TL):  $x < 0, y > 0$ .

Top right (TR):  $x > 0, y > 0$ .

Bottom right (BR):  $x > 0, y < 0$

Figures 7 and 8 show the normal and shear contributions, respectively, to the local traction and lift force along the pillar surface for different values of  $G^*$  and  $Re$  at  $\alpha = 5^\circ$ . Note that the normal contribution to the local traction and lift is dominated by the pressure forces; the normal component of the viscous stress is negligible (data not shown).

It can be seen from both figures that, at low  $Re$ , the traction and lift distributions are highly symmetric, which signifies the flow reversibility in the Stokes limit. Due to this symmetry, the surface integral over the lift distribution nearly vanishes and, thus,  $A \approx 0$ . Upon an increase of  $Re$ , the symmetry is broken in a nontrivial way, leading to a nonzero anisotropy. By definition, there is no lift generated by normal forces (Fig. 7) at the upstream and downstream points of the pillar where the surface normal is parallel to the flow direction ( $x$ -axis). Likewise, the lift generated by the shear forces (Fig. 8) identically vanishes at the top and bottom points of the pillar where the surface normal is parallel to the lift direction ( $y$ -axis).

Inspecting Fig. 7, we observe that, as  $Re$  increases, the normal component of the traction vector on the upstream side of the pillar becomes skewed toward the top side (from the BL to the TL quadrant). Two mechanisms contribute to this effect. First, as fluid decelerates significantly at the upstream stagnation point, pressure increases, leading to an increased normal component of the

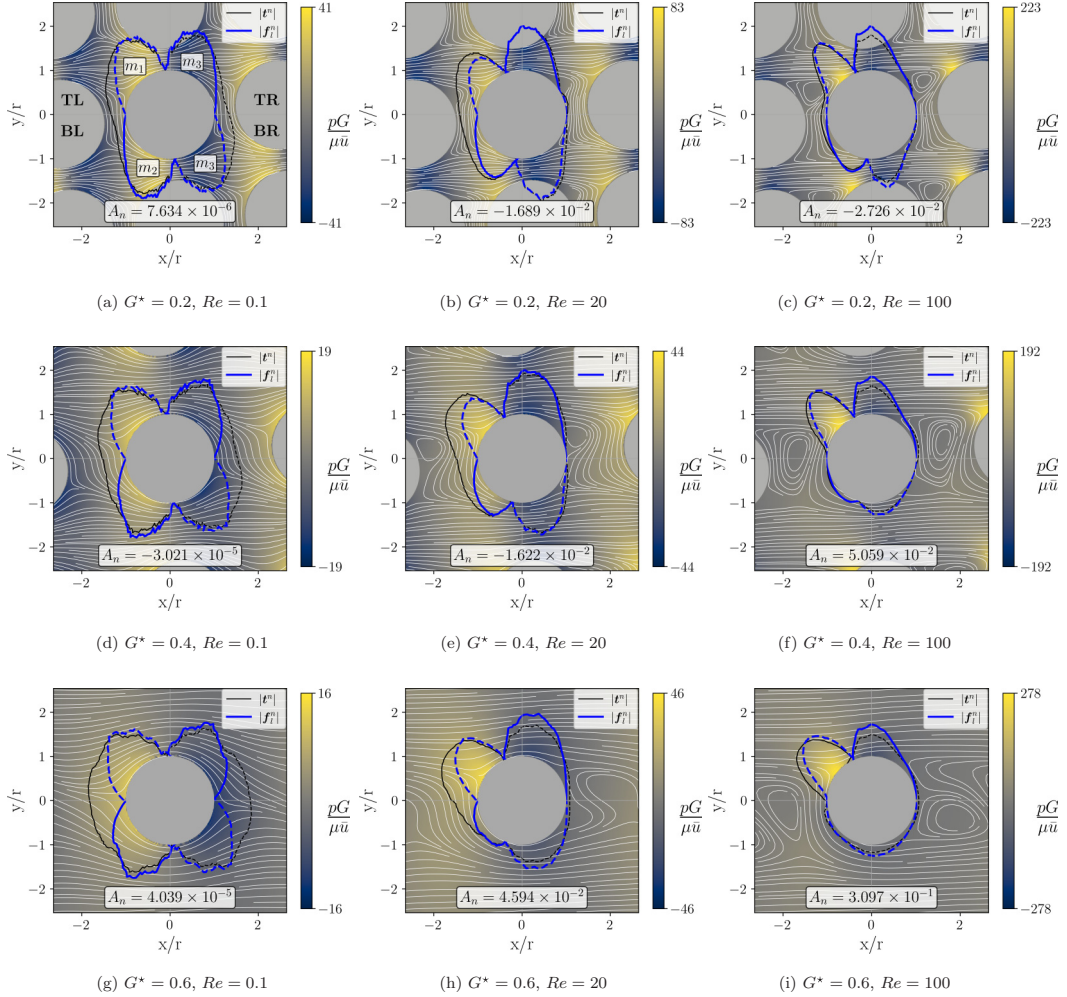


FIG. 7. Polar representation of the normal contribution to the traction (black) and lift (blue) along the pillar surface for (a)–(c)  $G^* = 0.2$ , (d)–(f)  $G^* = 0.4$ , and (g)–(i)  $G^* = 0.6$  at  $\alpha = 5^\circ$  for different values of  $Re$ . The average flow direction is along the  $x$ -axis. The traction and lift distributions are normalized by their maximum values. Positive values are shown as a solid line, negative values as a dashed line. The value of the normal contribution to the anisotropy is reported in each panel. Panel (a) also contains labels of the quadrants, and the labels for mechanisms associated with each region of the lift distribution, as referred to in Sec. III D. The normalized pressure field is shown as a color gradient.

traction vector on the pillar in the vicinity of the stagnation point (TL quadrant). Second, the pressure in the fluid near the BL part of the pillar decreases relative to the pressure magnitude in the other three quadrants. Thus, the normal component of the traction vector in the BL quadrant decreases. Both mechanisms contribute negatively to lift, leading to an increase in anisotropy, according to Eq. (8).

Further inspection of Fig. 7 reveals that, with increasing  $Re$ , the normal component of the traction vector in the BR quadrant becomes less negative than in the TR quadrant. This change in traction distribution is caused by the skewing of the velocity profile in the vertical gap (Fig. 4), which results in a higher velocity (and therefore lower pressure) near the top side of the pillar than near the bottom side. As a consequence, the net lift force increases, contributing to a decrease in anisotropy. The two

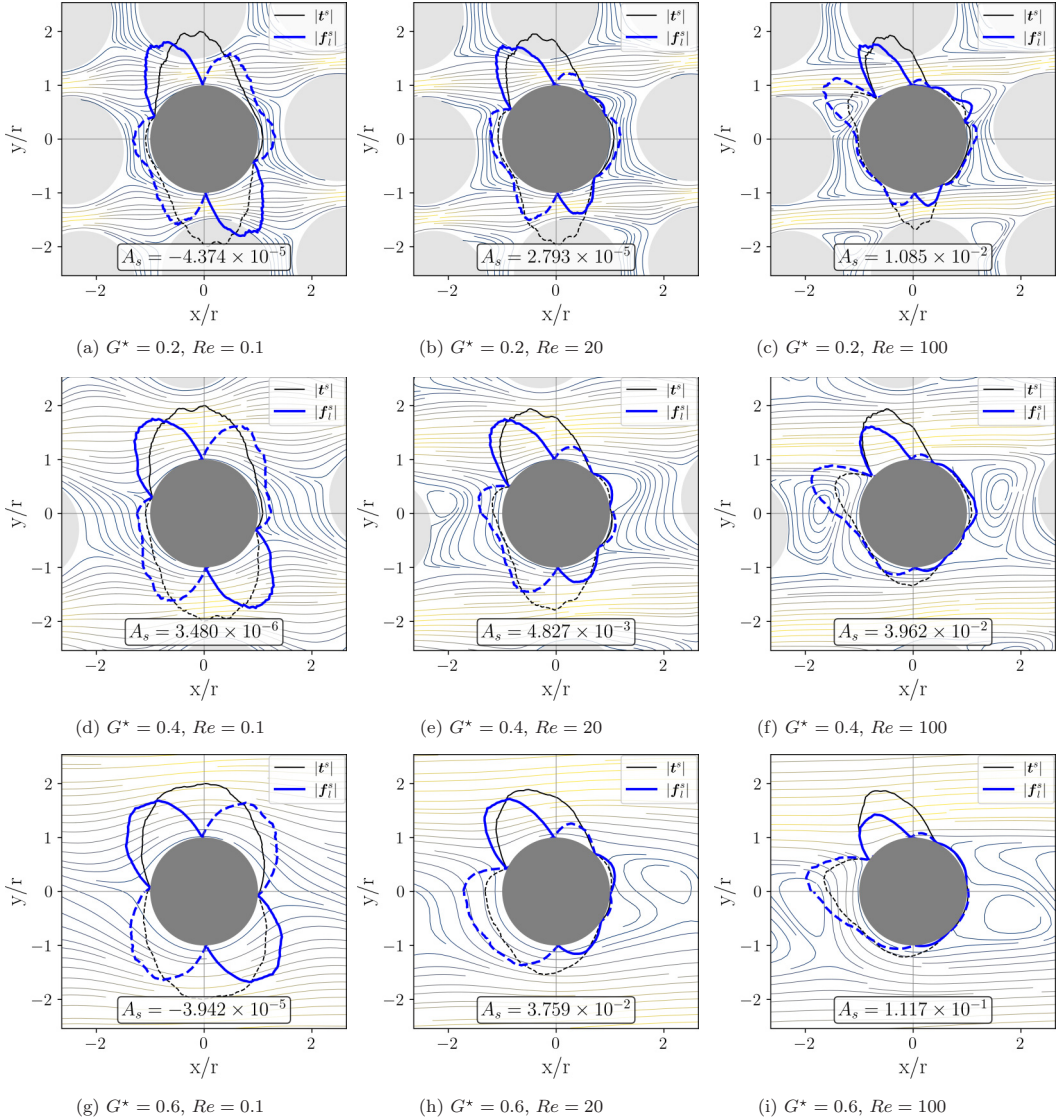


FIG. 8. Polar representation of the shear contribution to the traction (black) and lift (blue) along the pillar surface for (a)–(c)  $G^* = 0.2$ , (d)–(f)  $G^* = 0.4$ , and (g)–(i)  $G^* = 0.6$  at  $\alpha = 5^\circ$  for different values of  $Re$ . The average flow direction is along the  $x$ -axis. The traction and lift distributions are normalized by their maximum values. Positive values are shown as a solid line, negative values as a dashed line. The value of the shear contribution to the anisotropy is reported in each panel. The fluid flow is shown as streamlines using the same coloring as in Fig. 3.

identified effects—the role of the TL stagnation point and the skewed velocity profile in the vertical gap—oppose each other but do not cancel exactly. For  $Re > 5$ , outside the Stokes regime, there is a net change in anisotropy that can be positive or negative, and is particularly significant for larger  $G^*$ .

The picture is different for the contribution of the shear component of the traction vector to the lift (Fig. 8). For small  $Re$ , the shear component of the traction is largest around the top and bottom sides of the pillar but negligible at the upstream and downstream sides of the pillar. This observation

can be explained by the main flow through the vertical gap (in the positive  $x$ -direction) being fast (therefore creating a higher shear stress at the top and bottom sides of the pillar), while the lateral flow through the horizontal gap (in the negative  $y$ -direction) is relatively slow (therefore creating little shear stress).

Upon increasing  $Re$ , the lift associated with the shear stress is primarily determined by the fluid flowing around the pillar near the stagnation point in the TL quadrant, as can be seen clearly in the right column of Fig. 8. It is helpful to consider two primary contributions to the lift in the vicinity of the stagnation point: the shear stress caused by the clockwise flow along the top side of the pillar, and the shear stress caused by the counterclockwise flow around the upstream side of the pillar. The former tends to lift the pillar upward (contributing to negative anisotropy), while the latter tends to push the pillar downward (negative lift, contributing to positive anisotropy). Importantly, the shear stress of the clockwise flow is largest in a region where the tangential vector to the pillar surface is nearly parallel to the main flow direction ( $x$ -axis), hence shear forces generate hardly any lift. However, the shear stress of the counterclockwise flow is concentrated in a region where the surface tangent vector is essentially parallel to the lateral direction ( $y$ -axis), hence shear forces in this region contribute strongly to the lift.

For larger  $G^*$ , we can see that the traction caused by counterclockwise flow increases since the flow in this region is faster, and the high-speed flow region is pushed closer to the pillar surface than for smaller  $G^*$  (Fig. 3). Finally, since the flow in the vortex at the downstream side of the pillar is slow, there is hardly any lift generated by shear stresses in the vortex region.

In summary, we have identified several mechanisms that either increase or decrease lift and, therefore, decrease or increase anisotropy, all as a function of  $Re$  and  $G^*$  (and to a lesser degree of  $\alpha$ ):

- (i) Normal component of traction vector due to upstream stagnation point (TL quadrant):  $F_1^n \downarrow$ ,  $A^n \uparrow$ .
- (ii) Normal component of traction vector due to low pressure magnitude (BL quadrant):  $F_1^n \downarrow$ ,  $A^n \uparrow$ .
- (iii) Normal component of traction vector due to tilted horizontal velocity profile (TR and BR quadrants):  $F_1^n \uparrow$ ,  $A^n \downarrow$ .
- (iv) Shear component of traction vector due to clockwise flow along top side:  $F_1^s \uparrow$ ,  $A^s \downarrow$ .
- (v) Shear component of traction vector due to counterclockwise flow along upstream/bottom sides:  $F_1^s \downarrow$ ,  $A^s \uparrow$ .

Only mechanisms (iii) and (iv) contribute to a decrease in anisotropy. However, mechanism (iv) has been shown never to be stronger than mechanism (v), as the shear contribution to anisotropy is always positive [Figs. 6(d)–6(f)]. Therefore, the net effect of mechanisms (iv) and (v) always leads to an increase in anisotropy. Thus, we can conclude that the cause of the negative anisotropy for intermediate  $Re$  is mechanism (iii), the positive lift due to pressure forces caused by the skewed velocity profile.

To further quantify the influence of the tilted horizontal velocity profile [mechanism (iii)] on the sign of the anisotropy, we split the contribution of the normal component of the traction vector to the lift force distribution along the pillar into regions bounded by sign changes. From Fig. 7 we see that there are generally four distinct regions: two with a negative contribution to the total lift, primarily existing in the TL and BR quadrants, and two with a positive contribution in the TR and BL quadrants. We assume that the region occupying the TL quadrant is associated with mechanism (i), and that the region occupying the BL quadrant is associated with mechanism (ii). We further assume that the regions occupying the TR and BR quadrants are associated with mechanism (iii). Annotations of the regions of the lift distribution with the mechanism associated with them can be seen in Fig. 7(a) for reference.

We integrate the lift distribution associated with mechanisms (i) and (ii) to estimate their combined effect, and we do the same for the two regions associated with mechanism (iii). The results, nondimensionalized by  $\rho \bar{u}^2$ , are shown in Fig. 9. Values for  $Re = 100$  are not shown for  $G^* = 0.6$ , as the regions occupying the BL and BR quadrants merge together.

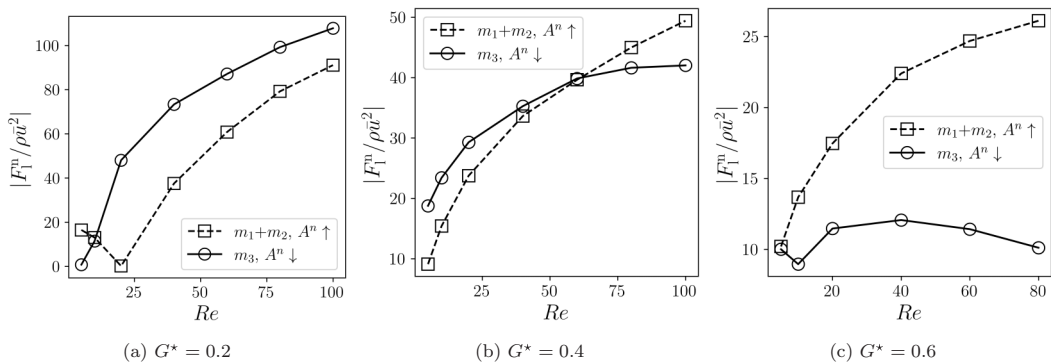


FIG. 9. Magnitude of normal lift force associated with the different mechanisms identified in Sec. III D. The sum of mechanisms (i) and (ii) ( $m_1$  and  $m_2$ ), associated with the upstream stagnation point and vertical flow and contributing to positive anisotropy, is compared with mechanism (iii) ( $m_3$ ), associated with the skewed horizontal velocity profile and contributing to negative anisotropy. When the solid line is above the broken line, we expect to see an overall negative value of the normal anisotropy,  $A^n$ . For  $G^* = 0.6$ , values are only plotted up to  $Re = 80$ , as the lift profile has only three zeros at  $Re = 100$ .

Figure 9 shows that, for  $G^* = 0.2$ , the mechanism associated with negative anisotropy dominates over the entire range of  $Re$  while both curves are close to each other, thus leading to a small negative anisotropy as found in Fig. 6(c). For  $G^* = 0.4$ , the mechanism associated with negative anisotropy dominates at low  $Re$  but begins to level off as  $Re$  increases, whereas the mechanisms associated with positive anisotropy increase more steadily, leading to the dominating mechanism swapping around  $Re = 60$ , which leads to the contribution of normal traction to the anisotropy becoming positive around  $Re = 60$  as seen in Fig. 6(c). Finally, for  $G^* = 0.6$ , the mechanism associated with positive anisotropy dominates for all values of  $Re$  and increases with  $Re$ , which can be seen as a steep increase of the contribution of normal traction to the anisotropy in Fig. 6(c).

Although the precise mechanisms underlying the observed dependencies on  $Re$  and  $G^*$  are currently unclear, it is evident that the relative effects of mechanisms (i)–(iii) differ based on these parameters, resulting in the observed shifts in anisotropy under varying conditions.

### E. Implication for real-world DLD devices

In an ideal DLD device with zero flow anisotropy, the background flow, on average, is exactly aligned with the direction of the applied pressure gradient, usually the device axis. Particles below the critical size follow the streamlines to leading order, resulting in zero lateral displacement along the device. Particles above the critical size are displaced laterally across the streamlines and pass through the device at a predictable angle relative to the flow. However, as has been shown previously in the work by Vernekar *et al.* [20], if anisotropy in a DLD device is nonzero, the background flow can become tilted relative to the applied pressure gradient. The effect of this tilting of the background flow is twofold. First, small particles that follow the streamlines have a nonzero lateral displacement relative to the applied pressure gradient. Second, the angle of displacement of larger particles is different from that which was expected assuming idealized flow. These effects can lead to the breakdown of the separation performance for a given device since particles may not end up in their expected downstream locations.

Our results demonstrate that flow anisotropy can arise in rotated-square pillar arrangements (which have previously been recommended due to their isotropic permeability in Stokes flow [20]) when fluid inertia is finite. Furthermore, we have shown that the degree of anisotropy is a nonlinear function of Reynolds number. This effect can cause problems for any experimentalist who attempts

to operate a rotated-square DLD device at throughputs high enough to trigger inertia-induced anisotropy.

To solve the problem caused by inertia-induced anisotropy in DLD, either by changes to the device design or by adapting the operating conditions, the mechanisms by which the anisotropy arises must be well understood. Thus, our new understanding of the mechanisms leading to inertia-induced anisotropy provides an essential step towards the goal of reliably running DLD devices at high throughput.

#### IV. CONCLUSIONS

Deterministic lateral displacement (DLD) is a relatively recent method for microfluidic particle separation. Although well understood in the Stokes regime, the performance of DLD devices operated with higher throughput, where inertia is not small, has not been sufficiently well characterized and analyzed. Earlier work has shown that, under some conditions, the flow in DLD devices can become anisotropic, i.e., the direction of flow can deviate from that of the applied driving force. Anisotropic flow in DLD devices leads to less predictable particle behavior and, thus, problems with particle separation.

We have investigated, via lattice-Boltzmann simulations, the onset and behavior of flow anisotropy of two-dimensional rotated-square DLD arrays in the inertial regime. We show that this geometry, which exhibits no anisotropy in the Stokes regime, can have either positive or negative anisotropy, depending on the Reynolds number ( $Re$ ), the reduced gap size ( $G^*$ ), and the array inclination angle ( $\alpha$ ). We find that anisotropy becomes significant for  $Re > 5$ , where inertial effects start to play an important role. The anisotropy increases strongly with  $Re$  for the largest gap size,  $G^* = 0.6$ , indicating that the fluid prefers to flow along the principal axis of the array. For smaller gaps,  $G^* = 0.4$  and  $0.2$ , anisotropy first becomes negative and only increases again at larger  $Re$ . We find that increasing  $\alpha$  increases the magnitude of the anisotropy, but does not significantly affect the overall behavior.

By analyzing the contributions of the normal and shear components of the traction vector to the local forces acting on the pillar surface, we identify several mechanisms that either increase or decrease anisotropy, as a function of  $Re$  and  $G^*$ . We show that the negative contributions to the anisotropy can be attributed purely to traction forces normal to the pillar surface. We suggest that this negative contribution to the anisotropy arises from an asymmetric tilting of the velocity profile between the pillars, which leads to a pressure differential along the axis orthogonal to the flow axis.

Our findings provide valuable insights into the anisotropic behavior of fluid flow over periodic square arrays of cylinders. Our work could be useful for the design of microfluidic devices and other applications where the control of fluid flow over periodic arrays of obstacles is important.

Since real DLD devices are 3D, and are influenced by the top and bottom walls as well as by the interaction of suspended particles with the flow field, we propose that future work should focus on 3D geometries including the effects of suspended particles *via* fluid-structure-interaction models, and we propose investigating how anisotropy can be controlled with different post shapes at finite inertia.

#### ACKNOWLEDGMENTS

This work was supported in part by the Carnegie Trust Vacation Scholarship scheme. T.K. received funding from the European Research Council (ERC) under the European Union's Horizon 2020 research and innovation program (No. 803553).

#### APPENDIX: INTERPOLATION-EXTRAPOLATION SCHEME

Figure 10 presents an illustration of the employed interpolation-extrapolation scheme.

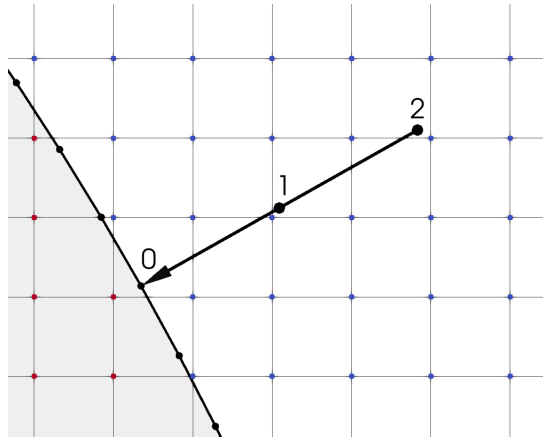


FIG. 10. Illustration of the employed interpolation-extrapolation scheme. Lattice points are shown in red (solid nodes) and blue (fluid nodes). Flow information at points 1 and 2 is bilinearly interpolated from the four nodes defining the surrounding voxels, respectively. The interpolated values are then linearly extrapolated to point 0 on the cylinder surface.

- 
- [1] P. Hu, W. Zhang, H. Xin, and G. Deng, Single cell isolation and analysis, *Front. Cell Dev. Biol.* **4**, 116 (2016).
- [2] L. R. Huang, E. C. Cox, R. H. Austin, and J. C. Sturm, Continuous particle separation through deterministic lateral displacement, *Science* **304**, 987 (2004).
- [3] C. I. Civin, T. Ward, A. M. Skelley, K. Gandhi, Z. Peilun Lee, C. R. Dosier, J. L. D’Silva, Y. Chen, M. J. Kim, J. Moynihan, X. Chen, L. Aurich, S. Gulnik, G. C. Brittain, D. J. Recktenwald, R. H. Austin, and J. C. Sturm, Automated leukocyte processing by microfluidic deterministic lateral displacement, *Cytometry Pt. A* **89**, 1073 (2016).
- [4] K. K. Zeming, R. Vernekar, M. T. Chua, K. Y. Quek, G. Sutton, T. Krüger, W. S. Kuan, and J. Han, Label-free biophysical markers from whole blood microfluidic immune profiling reveal severe immune response signatures, *Small* **17**, 2006123 (2021).
- [5] D. W. Inglis, J. A. Davis, R. H. Austin, and J. C. Sturm, Critical particle size for fractionation by deterministic lateral displacement, *Lab Chip* **6**, 655 (2006).
- [6] D. W. Inglis, N. Herman, and G. Vesey, Highly accurate deterministic lateral displacement device and its application to purification of fungal spores, *Biomicrofluidics* **4**, 024109 (2010).
- [7] H. N. Joensson, M. Uhlén, and H. A. Svahn, Droplet size based separation by deterministic lateral displacement- separating droplets by cell-induced shrinking, *Lab Chip* **11**, 1305 (2011).
- [8] J. A. Davis, Microfluidic separation of blood components through deterministic lateral displacement, Ph.D. thesis, Princeton University, Princeton NJ, 2008.
- [9] J. McGrath, M. Jimenez, and H. Bridle, Deterministic lateral displacement for particle separation: a review, *Lab Chip* **14**, 4139 (2014).
- [10] M. S. Wullenweber, J. Kottmeier, I. Kampen, A. Dietzel, and A. Kwade, Numerical study on high throughput and high solid particle separation in deterministic lateral displacement microarrays, *Processes* **11**, 2438 (2023).
- [11] A. Aghilinejad, M. Aghaamoo, and X. Chen, On the transport of particles/cells in high-throughput deterministic lateral displacement devices: Implications for circulating tumor cell separation, *Biomicrofluidics* **13**, 034112 (2019).
- [12] B. M. Dincau, A. Aghilinejad, T. Hammersley, X. Chen, and J.-H. Kim, Deterministic lateral displacement

- (DLD) in the high Reynolds number regime: high-throughput and dynamic separation characteristics, *Microfluid. Nanofluid.* **22**, 59 (2018).
- [13] Y. S. Lubbersen, M. A. I. Schutyser, and R. M. Boom, Suspension separation with deterministic ratchets at moderate Reynolds numbers, *Chem. Eng. Sci.* **73**, 314 (2012).
- [14] T. J. Bowman, G. Drazer, and J. Frechette, Inertia and scaling in deterministic lateral displacement, *Biomicrofluidics* **7**, 064111 (2013).
- [15] S. R. Reinecke, S. Blahout, T. Rosemann, B. Kravets, M. Wullenweber, A. Kwade, J. Hussong, and H. Kruggel-Emden, DEM-LBM simulation of multidimensional fractionation by size and density through deterministic lateral displacement at various Reynolds numbers, *Powder Technol.* **385**, 418 (2021).
- [16] B. M. Dincau, A. Aghilinejad, X. Chen, S. Y. Moon, and J.-H. Kim, Vortex-free high-Reynolds deterministic lateral displacement (DLD) via airfoil pillars, *Microfluid. Nanofluid.* **22**, 137 (2018).
- [17] Y. S. Lubbersen, J. P. Dijkshoorn, M. A. I. Schutyser, and R. M. Boom, Visualization of inertial flow in deterministic ratchets, *Separation Purification Technol.* **109**, 33 (2013).
- [18] T. Kulrattanarak, R. G. M. van der Sman, Y. S. Lubbersen, C. G. P. H. Schroën, H. T. M. Pham, P. M. Sarro, and R. M. Boom, Mixed motion in deterministic ratchets due to anisotropic permeability, *J. Colloid Interface Sci.* **354**, 7 (2011).
- [19] S.-C. Kim, B. H. Wunsch, H. Hu, J. T. Smith, R. H. Austin, and G. Stolovitzky, Broken flow symmetry explains the dynamics of small particles in deterministic lateral displacement arrays, *Proc. Natl. Acad. Sci. USA* **114**, E5034 (2017).
- [20] R. Vernekar, T. Krüger, K. Louthback, K. Morton, and D. W. Inglis, Anisotropic permeability in deterministic lateral displacement arrays, *Lab Chip* **17**, 3318 (2017).
- [21] A. Hochstetter, R. Vernekar, R. H. Austin, H. Becker, J. P. Beech, D. A. Fedosov, G. Gompper, S.-C. Kim, J. T. Smith, G. Stolovitzky, J. O. Tegenfeldt, B. H. Wunsch, K. K. Zeming, T. Krüger, and D. W. Inglis, Deterministic lateral displacement: Challenges and perspectives, *ACS Nano* **14**, 10784 (2020).
- [22] D. L. Koch and A. J. C. Ladd, Moderate Reynolds number flows through periodic and random arrays of aligned cylinders, *J. Fluid Mech.* **349**, 31 (1997).
- [23] A. Dybbs and R. V. Edwards, A new look at porous media fluid mechanics—Darcy to turbulent, in *Fundamentals of Transport Phenomena in Porous Media*, edited by J. Bear and M. Yavuz Corapcioglu, NATO ASI Series (Springer, Dordrecht, 1984), pp. 199–256.
- [24] M. Quintard and S. Whitaker, Transport in ordered and disordered porous media: volume-averaged equations, closure problems, and comparison with experiment, *Chem. Eng. Sci.* **48**, 2537 (1993).
- [25] D. Natarajan and T. Van Nguyen, A two-dimensional, two-phase, multicomponent, transient model for the cathode of a proton exchange membrane fuel cell using conventional gas distributors, *J. Electrochem. Soc.* **148**, A1324 (2001).
- [26] H. Bazzyar, P. Lv, J. A. Wood, S. Porada, D. Lohse, and R. G. H. Lammertink, Liquid–liquid displacement in slippery liquid-infused membranes (SLIMs), *Soft Matter* **14**, 1780 (2018).
- [27] M. Kumar, J. S. Guasto, and A. M. Ardekani, Transport of complex and active fluids in porous media, *J. Rheol.* **66**, 375 (2022).
- [28] A. G. Hunt and M. Sahimi, Flow, transport, and reaction in porous media: Percolation scaling, critical-path analysis, and effective medium approximation, *Rev. Geophys.* **55**, 993 (2017).
- [29] A. Tamayol, A. Khosla, B. L. Gray, and M. Bahrami, Creeping flow through ordered arrays of microcylinders embedded in a rectangular minichannel, *Int. J. Heat Mass Transf.* **55**, 3900 (2012).
- [30] T. O. M. Forslund, I. A. S. Larsson, H. Lycksam, J. G. I. Hellström, and T. S. Lundström, Non-Stokesian flow through ordered thin porous media imaged by tomographic-PIV, *Exp. Fluids* **62**, 46 (2021).
- [31] T. O. M. Forslund, I. A. S. Larsson, J. G. I. Hellström, and T. S. Lundström, Steady-state transitions in ordered porous media, *Transp. Porous Media* **149**, 551 (2023).
- [32] A. Xu, T. S. Zhao, L. Shi, and J. B. Xu, Lattice Boltzmann simulation of mass transfer coefficients for chemically reactive flows in porous media, *J. Heat Transf.* **140**, 052601 (2018).
- [33] D. Lasseux, A. A. Abbasian Arani, and A. Ahmadi, On the stationary macroscopic inertial effects for one phase flow in ordered and disordered porous media, *Phys. Fluids* **23**, 073103 (2011).
- [34] T. H. Chakrapani, H. Bazzyar, R. G. H. Lammertink, S. Luding, and W. K. den Otter, The permeability



- of pillar arrays in microfluidic devices: An application of Brinkman's theory towards wall friction, [Soft Matter](#) **19**, 436 (2023).
- [35] K. Ahasan, C. M. Landry, X. Chen, and J.-H. Kim, Effect of angle-of-attacks on deterministic lateral displacement (DLD) with symmetric airfoil pillars, [Biomed. Microdev.](#) **22**, 42 (2020).
- [36] T. Krüger, H. Kusumaatmaja, A. Kuzmin, O. Shardt, G. Silva, and E. M. Viggien, *The Lattice Boltzmann Method: Principles and Practice*, Graduate Texts in Physics (Springer International, Switzerland, 2017).
- [37] S. Succi, *The Lattice Boltzmann Equation for Fluid Dynamics and Beyond* (Clarendon, Oxford, England, 2001).
- [38] P. L. Bhatnagar, E. P. Gross, and M. Krook, A model for collision processes in gases. I. small amplitude processes in charged and neutral one-component systems, [Phys. Rev.](#) **94**, 511 (1954).
- [39] Z. Guo, C. Zheng, and B. Shi, Discrete lattice effects on the forcing term in the lattice Boltzmann method, [Phys. Rev. E](#) **65**, 046308 (2002).
- [40] A. J. C. Ladd, Numerical simulations of particulate suspensions via a discretized Boltzmann equation. Part 1. Theoretical foundation, [J. Fluid Mech.](#) **271**, 285 (1994).